



# Nonlinear simulations of wave-induced motions of a freely floating body using WCSPH method

Bing Ren <sup>a,\*</sup>, Ming He <sup>a</sup>, Ping Dong <sup>b</sup>, Hongjie Wen <sup>a</sup>

<sup>a</sup> The State Key Laboratory of Coastal and Offshore Engineering, Dalian University of Technology, Dalian 116024, China

<sup>b</sup> School of Engineering, Physics and Mathematics, University of Dundee, DD1 4HN, United Kingdom



## ARTICLE INFO

### Article history:

Received 10 September 2014

Received in revised form

20 November 2014

Accepted 15 December 2014

Available online 13 January 2015

### Keywords:

SPH

Floating body

Fluid body interaction

Nonlinear wave

## ABSTRACT

Nonlinear interactions between waves and floating bodies are investigated using the weakly compressible Smoothed Particle Hydrodynamic (WCSPH) method. An improved algorithm based on the dynamic boundary particles (DBPs) is proposed to treat the moving boundary of the floating body. The force exerted on the floating body boundary particle by the particles surrounding it is evaluated using the volume integration of the stress tensors obtained from the momentum equation in its compact support. The improved WCSPH model is validated by the experimental results. The numerical test cases of the vertical oscillation of a rectangular box, the damped rolling oscillation of a floating box and the wave forces on a fixed rectangular box are then carried out to demonstrate the performance of the proposed model. Finally the evolution in time of the dynamic response of the freely floating body under nonlinear waves are discussed and compared with experimental results.

© 2014 Elsevier Ltd. All rights reserved.

## 1. Introduction

The interactions between waves and floating bodies have been studied extensively in naval, ocean and coastal engineering. The early established methods are often analytical and use frequency-domain analyses based on potential flow theories, neglecting the fluid viscosity and the nonlinear effect. They are therefore limited to solving the motion of a floating body of simple shape in small-amplitude waves. As for floating bodies with complex shape, Boundary Element Method (BEM) was used to obtain the periodic steady solutions by solving numerically a boundary value problem in the frequency domain. However, although these frequency domain models are powerful and accurate in solving linear problems, they perform much less well when the interactions between waves and floating bodies become significantly nonlinear.

With the advancement of computational fluid dynamics, a number of nonlinear numerical models in time domain including BEM models have been developed. For the weakly nonlinear problems, BEM models for the second-order or higher-order wave action on a floating body are developed by many researchers [1]. For the nonlinear interactions between large waves and rigid bodies, Longuet-Higgins and Cokelet [2] introduced the Mixed Eulerian-Lagrangian (MEL) method based on BEM to deal with

the instantaneous free surface and the wet body boundary. This approach was followed and further developed to study the nonlinear interactions between the waves and the moored floating bodies [3–6]. However, as the MEL method uses moving girds and Lagrangian algorithm to treat the free surface, it fails when extreme deformation of the free surface occurs and it is also unable to deal with the large-amplitude motions of floating bodies inside the fluid domain.

Another problem with these models which are based on the potential flow theory is that they are not suitable when viscous or turbulence effects are significant. To address this problem, a large number of models based on the NS or RANS equations using either the finite difference method or the finite volume method (FVM) have been developed together with various interface-capturing techniques such as the Level Set function, the Volume of Fluid and others. For the nonlinear fluid solid interaction, the full coupling between the fluid and the rigid body requires adaptive and moving mesh methods to keep tracking continuously of the interface between the fluid and structure. Hadžić [7] employ a body-fitted mesh using a combination of mesh motion, mesh deformation, and sliding mesh interfaces to predict the multi-degree-of-freedom motions of a free floating rectangular body based on FVM. Jung [8] simulated the coupled interaction between a wave and a free-rolling rectangular structure using FVM and the similar mesh technique as that of Hadžić [7]. Hu and Kashiwagi [9] developed the Constrained Interpolation Profile (CIP)-based Cartesian grid method to investigate the free-sway motion of a floating body with rectangular section shape which is represented by a virtual particle method.

\* Corresponding author. Tel.: +86 13052735468.

E-mail addresses: [bren@dlut.edu.cn](mailto:bren@dlut.edu.cn) (B. Ren), [hemingdut@gmail.com](mailto:hemingdut@gmail.com) (M. He), [p.dong@dundee.ac.uk](mailto:p.dong@dundee.ac.uk) (P. Dong), [hongjiew@126.com](mailto:hongjiew@126.com) (H. Wen).

The above methods are Eulerian and rely on complicated algorithms to capture the instantaneous free surface, which can be difficult and inaccurate when the deformation of free surface is large or the shape of the floating body is complicated. In comparison, Lagrangian meshless methods such as SPH method [10] are clearly advantageous and have seen significant development in recent years. Monaghan [11] used WCSPH to investigate the entry of a box traveling down a slope into water. Doring [12] developed an accurate evaluation approach of fluid force on solid boundaries to resolve the water entry and floating-body/wave interaction problems. Shao and Gotoh [13] developed the ISPH method to study the motion of a floating curtain wall under the action of a progressive wave. Omidvar [14] enhanced SPH efficiency with the variable particle mass technique to model a 3D floating body motion. Hashemi [15] used the WCSPH method along with a modification to the continuity equation to investigate the motion of two freely falling solid bodies in a channel. Antuono [16] proposed the  $\delta$ -SPH model by adding an artificial diffusive term into the continuity equation to simulate gravity waves propagating in a basin with varied nonlinearities, which is then further developed to simulate the interaction between water waves and floating bodies of complex geometries [17].

The imposition of appropriate solid boundary conditions in SPH model is of primary importance to ensure a smooth and accurate pressure field around the solid surface. In the literature there mainly exists three solid boundary treatment methods, i.e. dynamic boundary [18,19], mirror particle boundary [20,21] and repulsive forces boundary [22–24]. Regarding the moving solid boundary of a floating body, another difficulty is the accurate estimation of the forces exerted on the moving body by the surrounding water particles. Oger [21] and Liu [25] employed the mirror particle method to enforce a free-slip boundary condition on the moving solid surface. The external fluid forces are evaluated by pressure integration of the fluid particles in the vicinity of the solid body boundary. Although this approach produces accurate results, it can be computationally expensive as reported by Shao [26] and may become unwieldy for corners or other geometrically complex solid surfaces [27]. An improved mirror particle technique based on fixed ghost particles was developed by Marrone [28] and Bouscasse [17]. The global fluid loads on moving boundaries are obtained through volume integrals over the ghost particle domain. The fixed ghost particles technique allows for a simple treatment of complex geometry that ensures both efficiency and accuracy at the expense of a moderately increased spatial resolution. Kajtar and Monaghan [29] used a set of boundary particles which exert repulsive forces to the neighboring fluid particles to treat the boundaries of swimming linked bodies. The sum of the counter forces on the boundary particles of a body gives the force on that body due to the fluid. However, it is difficult to determine the proper repulsive force function as pointed out by Monaghan and Kajtar [27].

There are generally two categories of treatments of the solid motion in SPH method. One category as used by Liu [25] and Bouscasse [17] is to treat structure as strictly solid boundary and the external forces are evaluated by integrating pressures at the boundary particles. The solid motion is modeled by the Newton's law of motion. This treatment is more straightforward in a particle approach. Another category treats the solid as deformable fluids [13] and the rigid motion is calculated based on the conservation of momentum between the fluid and solid particles. With this method, the pressure integration over the solid boundary is avoided to reduce the negative effect of the pressure fluctuations of boundary particles. This method is not straightforward and may result in some inconsistency of the fluid particles near the corner of a rotating body.

In the present study, an algorithm based on the dynamic boundary particles (DBPs) presented by Dalrymple and Knio [18] is

developed to treat the moving boundary of the floating body. Although DBPs does not require specifying the repulsive force function as the conventional repulsive boundary treatment does [23] and it cost much less CPU time than the mirror particle approach does, using DBPs to reproduce the solid boundary can sometimes give rise to anomalously high density gradients near the solid boundary [30] and result in unstable pressure field or very large unphysical boundary layers. In addition, as pointed out by Monaghan and Kajtar [27], when fluid particles moving away from DBPs, the apparent density and pressure of DBPs decreases, and consequently the fluid particles near the boundary can feel a spurious attraction from the DBPs. Therefore, a formulation to correct the pressure of DBPs is proposed to remove the spurious numerical effects near the solid boundary. A 2D fully nonlinear numerical wave tank (NWT) is developed using the WCSPH and the improved boundary treatment. The nonlinear interactions between large waves and freely floating rectangular box with up to three degrees of freedom are investigated by the NWT.

The paper is organized as follow: Firstly, the methodology including the governing equations of WCSPH model, solid boundary treatment method, equations of the motion of the rigid body and time stepping is presented. Next, the experiment setup of the validation tests is presented. Then the test cases of the vertical oscillation of a rectangular box, the damped rolling oscillation of a floating box, the water entry of a cylinder section and the wave forces on a fixed rectangular box are simulated to demonstrate the performance of the proposed model. Finally, the motions of a freely floating body under nonlinear waves are studied using the proposed model and validated by the experimental data.

## 2. Methodology

### 2.1. SPH formulation for the fluid flow

In the present work, the motion of the fluid is governed by the mass and momentum conservation equations as:

$$\frac{D\rho}{Dt} = -\rho \nabla \cdot \mathbf{u} \quad (1)$$

$$\frac{D\mathbf{u}}{Dt} = -\frac{1}{\rho} \nabla p + \mathbf{g} \quad (2)$$

where  $\rho$  is the density of the fluid,  $\mathbf{u}$  is the velocity vector,  $p$  is the pressure and  $\mathbf{g}$  is the gravitational acceleration.

In the WCSPH method, the pressure is determined through solving an equation of state. Following Monaghan and Kos [23], the frequently equation of state is

$$p = B \left[ \left( \frac{\rho}{\rho_0} \right)^\gamma - 1 \right] \quad (3)$$

where  $\gamma = 7$ ;  $\rho_0$  is a reference density,  $\rho_0 = 1000 \text{ kg/m}^3$ ;  $B = c_0^2 \rho_0 / \gamma$ ,  $c_0^2 = 200gd$ ,  $c_0$  is the speed of sound at the reference density and chosen to keep the relative density fluctuation  $\delta\rho/\rho$  less than 0.01, so that the fluid is nearly incompressible;  $d$  is the water depth.

The SPH formulation of Eqs. (1) and (2) can be written as:

$$\frac{d\rho_i}{dt} = \rho_i \sum_{j=1}^N \frac{m_j}{\rho_j} (\mathbf{u}_i - \mathbf{u}_j) \cdot \nabla_i W_{ij} \quad (4)$$

$$\frac{d\mathbf{u}_i}{dt} = -\sum_{j=1}^N m_j \left( \frac{p_i}{\rho_i^2} + \frac{p_j}{\rho_j^2} + \Pi_{ij} \right) \nabla_i W_{ij} + \mathbf{g} \quad (5)$$

In the above equations, subscripts  $i$  donates the target particle and subscripts  $j$  donates the neighboring particle within the support of  $i$ .  $N$  is the total number of the neighboring particles in the

support of  $i$ .  $m$  is the mass.  $W_{ij}$  is the kernel function. In this paper, a quintic kernel suggested by Wendland [31] is used:

$$W_{ij} = \frac{7}{4\pi h^2} \left(1 - \frac{q}{2}\right)^4 (2q + 1) \quad 0 \leq q \leq 2 \quad (6)$$

where  $q = \Delta r_{ij}/h$ ,  $\Delta r_{ij}$  is the distance between particles  $i$  and  $j$ ,  $h$  is the smoothing length.

The viscosity of real fluid is neglected and an artificial viscosity term  $\Pi_{ij}$  is added in the Eq. (5) to produce a shear and bulk viscosity [32].  $\Pi_{ij}$  is given by

$$\Pi_{ij} = \begin{cases} \frac{-\alpha_\Pi \bar{c}_{ij} \mu_{ij} + \beta_\Pi \mu_{ij}^2}{\bar{\rho}_{ij}} & \mathbf{u}_{ij} \cdot \mathbf{r}_{ij} < 0 \\ 0 & \mathbf{u}_{ij} \cdot \mathbf{r}_{ij} \geq 0 \end{cases} \quad (7)$$

where  $\mu_{ij} = h \mathbf{u}_{ij} \cdot \mathbf{r}_{ij} / (\mathbf{r}_{ij}^2 + \varphi^2)$ ,  $\bar{c}_{ij} = 0.5(c_i + c_j)$ ,  $\bar{\rho}_{ij} = 0.5(\rho_i + \rho_j)$ ,  $\mathbf{u}_{ij} = \mathbf{u}_i - \mathbf{u}_j$ ,  $\mathbf{r}_{ij} = \mathbf{r}_i - \mathbf{r}_j$ ,  $\varphi = 0.01 h$ ,  $c$  is the speed of sound.  $\alpha_\Pi$  and  $\beta_\Pi$  are empirical parameters that can be adjusted as required for each problem.

In order to smooth out the high frequency fluctuations of the particle density and pressure field, a Shepard filter [33] is used to renormalize the density field every 20-time steps:

$$\rho_i = \frac{\sum_j m_j W_{ij}}{\sum_j W_{ij} \frac{m_j}{\rho_j}} \quad (8)$$

The movements of particles are obtained by using the XSPH variant [34]

$$\frac{d\mathbf{r}_i}{dt} = \mathbf{u}_i + \varepsilon \sum_{j=1}^N \frac{m_j}{\bar{\rho}_{ij}} (\mathbf{u}_j - \mathbf{u}_i) W_{ij} \quad (9)$$

where  $\varepsilon$  is taken as 0.3 and the kernel is the same quintic kernel as used in calculating the acceleration. The last term on the right hand side of the equation brings the particle velocity closer to the average velocity in its neighborhood, and thus reduces the particle disorder. However, moving the particles with the smoothed velocities may result in the nonconservation of energy [35]. For this reason  $\varepsilon$  is taken as small as possible to reduce the negative effect of smoothed velocities.

## 2.2. Boundary treatment

As discussed in introduction, the kernel truncation problem near the solid boundary can usually generate unrealistic pressure fluctuation or result in the fluid particles penetrating the solid wall even with the kernel renormalized treatment. It is therefore necessary to implement specific solid boundary treatment to ensure a fairly smooth and accurate pressure field around the solid surface and prevent fluid particles from penetrating into the impermeable boundary.

In the present work, the fixed solid boundary and the wave maker boundary are treated using the dynamic boundary particles (DBPs), which is proposed by Dalrymple and Knio [18] and validated by Crespo [19]. The dynamic boundary particles follow the same equations of continuity and state as the fluid particles, but they do not follow the momentum equations and the XSPH variant. The positions of the fixed boundary particles remain unchanged and that of the wave maker particles follows the solution of the propagating waves. The most significant advantage of DBPs is its computational simplicity, since it is far easier to specify irregular boundaries by placing double rows of particles than to specify repulsive force

function as in [27] and it does not need additional programming and computations.

For the moving solid boundary of a floating body, a technique similar to the DBPs is proposed here to treat the interaction between the fluid and the solid. Although the movements of boundary particles do not follow the momentum equation of fluid, the evaluation of the forces exerted on the boundary particle by the particles in its neighborhood is obtained by the volume integration of the stresses tensor from the momentum equation. Thus, the forces on boundary particle  $i$  exerted by the neighboring particles are:

$$\mathbf{f}_i = m_i \frac{d\mathbf{u}_i}{dt} = m_i \left[ -\sum_{j=1}^N m_j \left( \frac{p'_i}{\rho_i^2} + \frac{p_j}{\rho_j^2} + \Pi_{ij} \right) \nabla_i W_{ij} + \mathbf{g} \right] \quad (10)$$

where  $p'_i$  and  $\rho'_i$  are the corrected pressure and density of the boundary particle, and the corrected pressure in Eq. (10) is obtained via the equation of state.

The boundary particles are placed in two rows on the fixed walls of the NWT or the moving solid walls of the floating body as illustrated in Fig. 1.

When enforcing the original DBPs on the solid boundary, the presence of the DBPs inside the computational domain can cause anomalously high density gradients near the DBPs [30], which can result in spurious high-frequency pressure oscillations and large unphysical boundary layers appear in the flow near the solid wall due to the large pressure gradient between the fluid and boundary particles. Gómez-Gesteira [30] buffered the calculated density to minimize the spurious effects.

Here the calculated densities of DBPs  $\rho_i$  from Eq. (4) are buffered by the mean densities of fluid particles  $\rho_{j-\text{avg}}$  in their kernel supports to reduce the spurious effects:

$$\rho'_i = \chi \rho_i + (1 - \chi) \rho_{j-\text{avg}} \quad (11)$$

In Eq. (11),  $\chi$  is chosen to be 0.2 and  $\rho_{j-\text{avg}}$  is calculated by:

$$\rho_{j-\text{avg}} = \frac{1}{N} \sum_{j=1}^N \left( \rho_j + \frac{\partial \rho_j}{\partial z} (z_j - z_i) \right) \quad (12)$$

where  $\rho_j$  is the density of fluid particle  $j$  in the vicinity of DBPs,  $N$  is the number of fluid particles in the kernel support,  $z_j$  and  $z_i$  are the vertical positions of the fluid particle and the boundary particle, respectively. The correction term  $\partial \rho_j / \partial z (z_j - z_i)$  is added to compensate the effects of truncated compact support. In the present work, only the correction concerning the hydrostatic pressure is included.

Substituting Eq. (3) into Eq. (12), the corrected density of the boundary particle becomes

$$\rho'_i = \chi \rho_i + (1 - \chi) \frac{1}{N} \sum_{j=1}^N \left( \rho_j + \frac{\rho_0^2 g}{7B} \left( \frac{\rho}{\rho_0} \right)^{-6} (z_j - z_i) \right) \quad (13)$$

## 2.3. Motion of floating body

The motion of the floating body is given by the equations of rigid body dynamics. Following the Newton's second law of motion, the translation motion of the center of mass and the rotation of the rigid body are given by

$$M \frac{d\mathbf{V}}{dt} = \mathbf{F} + \mathbf{Mg} \quad (14)$$

$$I \frac{d\boldsymbol{\Omega}}{dt} = \mathbf{T} \quad (15)$$

where  $M$  and  $I$  are the mass and the moment of inertia of the floating body, respectively.  $\mathbf{V}$  and  $\boldsymbol{\Omega}$  are the linear velocity and the angular

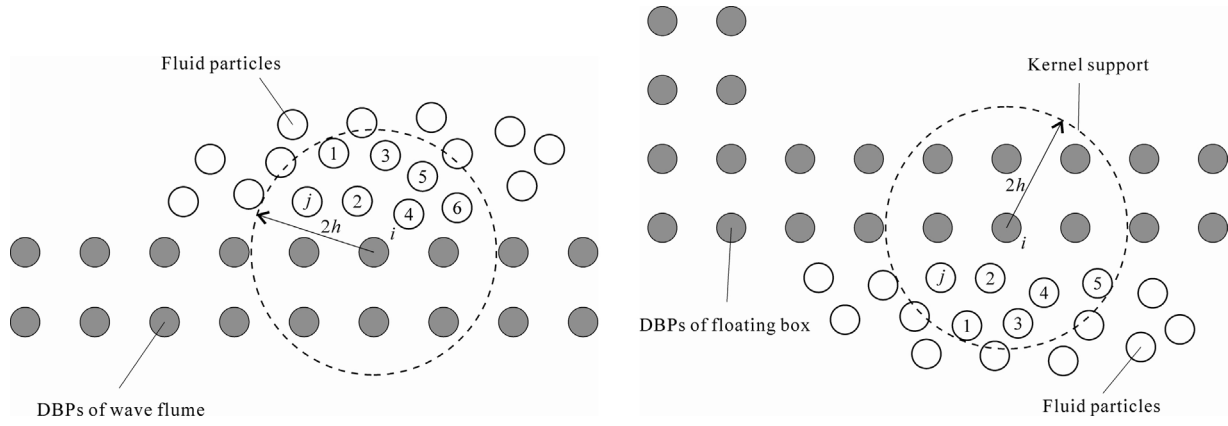


**Fig. 1.** Sketch of the boundary treatments. Left: DBPs of the NWT. Right: DBPs of the floating body.

velocity of the center of mass, respectively.  $\mathbf{F}$  and  $\mathbf{T}$  are the global hydrodynamic force and torque acting on the floating body.

The boundary of the floating body is described by a series of boundary particles. The force exerted by fluid particle on a boundary particle can be calculated with Eq. (10). By summing the forces exerted on the whole boundary particles (consisting of two rows), the global force  $\mathbf{F}$  and torque  $\mathbf{T}$  on the floating body can be evaluated. So the linear and angular equations of motion (Eqs. (14)~(15)) are rewritten as

$$M \frac{d\mathbf{V}}{dt} = \sum_{i \in \text{DBPs}} \mathbf{f}_i + M\mathbf{g} \quad (16)$$

$$I \frac{d\Omega}{dt} = \sum_{i \in \text{DBPs}} (\mathbf{r}_i - \mathbf{R}_0) \times \mathbf{f}_i \quad (17)$$

where  $\mathbf{f}_i$  is the hydrodynamics force acting on the boundary particle  $i$ ,  $\mathbf{R}_0$  is the position vector of the center of mass.

The boundary particles of the floating body move as parts of the rigid body, the velocity of a boundary particle is given as follows:

$$\frac{d\mathbf{r}_i}{dt} = \mathbf{V} + \boldsymbol{\Omega} \times (\mathbf{r}_i - \mathbf{R}_0) \quad (18)$$

#### 2.4. Time stepping

In this paper, the field variables  $\phi_i \equiv \{\rho_i, \mathbf{u}_i, \mathbf{r}_i\}$  are updated using a predictor–corrector scheme. The values of the variables at the half time step are predicted by

$$\phi_i^{n+1/2} = \phi_i^n + \frac{\Delta t}{2} \left( \frac{d\phi_i^n}{dt} \right) \quad (19)$$

These values are then corrected according to

$$\phi_i^{n+1/2} = \phi_i^n + \frac{\Delta t}{2} \left( \frac{d\phi_i^{n+1/2}}{dt} \right) \quad (20)$$

Finally, the values of the variables at time step  $n+1$  are calculated using the corrected  $\phi_i^{n+1/2}$

$$\phi_i^{n+1} = 2\phi_i^{n+1/2} - \phi_i^n \quad (21)$$

In the next step, the global fluid force on the floating body is obtained by summing up the force calculated by Eq. (10), followed by updating the position of the body by Eqs. (16) and (17).

Based on the Courant condition, the viscous diffusion term and the force terms, the time step  $\Delta t$  in the numerical model is calculated according to the following equation:

$$\Delta t = 0.2 \cdot \min(\Delta t_c, \Delta t_f) \quad (22)$$

In Eq. (22),  $\Delta t_c$  combines the Courant and viscosity conditions [23], which takes the form

$$\Delta t_c = \min_i \frac{h}{c_i + \max_j \left| \frac{h \mathbf{u}_{ij} \cdot \mathbf{r}_{ij}}{\mathbf{r}_{ij}^2} \right|} \quad (23)$$

$\Delta t_f$  is used to prevent fluid particles from penetrating the boundaries and given by

$$\Delta t_f = \min_i \sqrt{\frac{h}{|\mathbf{f}_i/m_i|}} \quad (24)$$

### 3. Experimental setup

An experiment for the validation of the proposed model was carried out in a wave flume at Dalian University of Technology. A sketch of the experimental setup is shown in Fig. 2. The flume is 23 m long and 0.44 m wide with initial water depth 0.4 m. A piston-type wave maker is set on the left-hand side of the flume and a wave absorber is placed on the other side. A freely floating rectangle box is placed in the middle of the flume. The box is made of 8-mm thick Perspex sheets and can be regarded as rigid body. The width  $B_f$  and the height  $H_f$  of the box are 0.3 m and 0.2 m, respectively. A total of 2 cm gap is kept between the lateral sides of the box and the sidewalls of the flume, so there is hardly any resistance to restrict the 2D free-floating motion. A separate space is constructed in the middle of length direction using two vertical glass plates and filled in full with granular materials as counterweight. The counterweight is pre-calculated to make the box half-immersed in water (i.e. an average density of 500 kg/m<sup>3</sup>).

A Charge-coupled Device (CCD) camera (Model: UP-930 from UNIQ Vision, Inc.; Resolution: 1024 × 1024 pixels; Frame Rate: 30 fps) is used to capture the real-time motions of the free-floating box and ambient wave surface. The camera focuses on the centroid of the box and a 1.2 m × 1.2 m area is monitored. Given the resolution of the camera, each pixel in the generating images represents 1.17 mm in actual size. The error of data in the experiment is within ±1.17 mm.

The experiment is conducted in a dark environment, and the light source is provided by the iodine-tungsten hanged on top of the flume (see the right plot of Fig. 2) to enhance the image contrast.

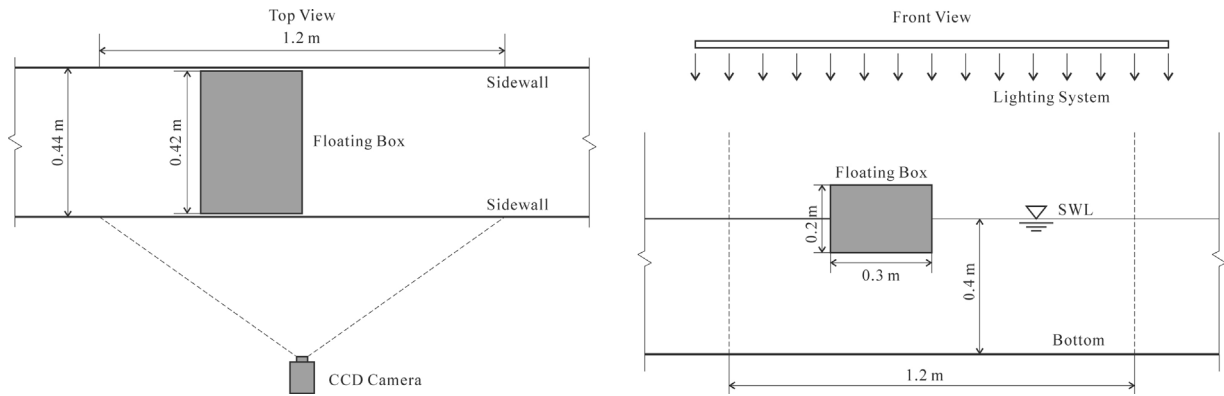


**Fig. 2.** Sketch of experimental setup. Left: top view. Right: front view.

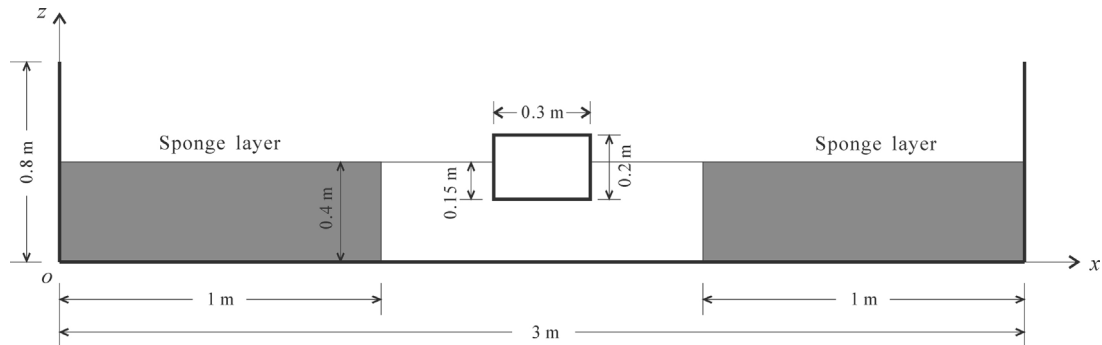


**Fig. 3.** Sketch of the vertical oscillating box.

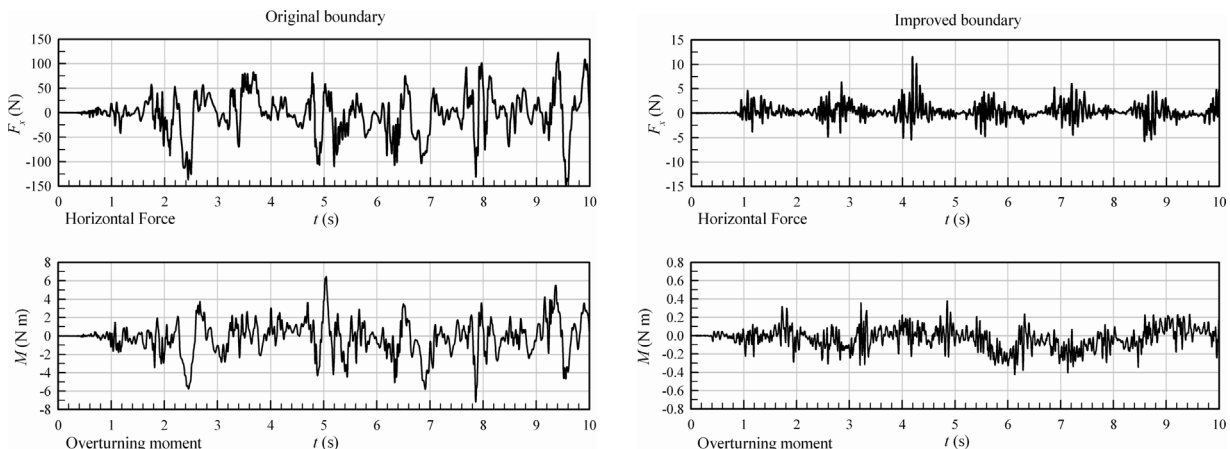


**Fig. 4.** Horizontal force and overturning moment on the vertically oscillating box. Left: original DBPs. Right: improved DBPs.

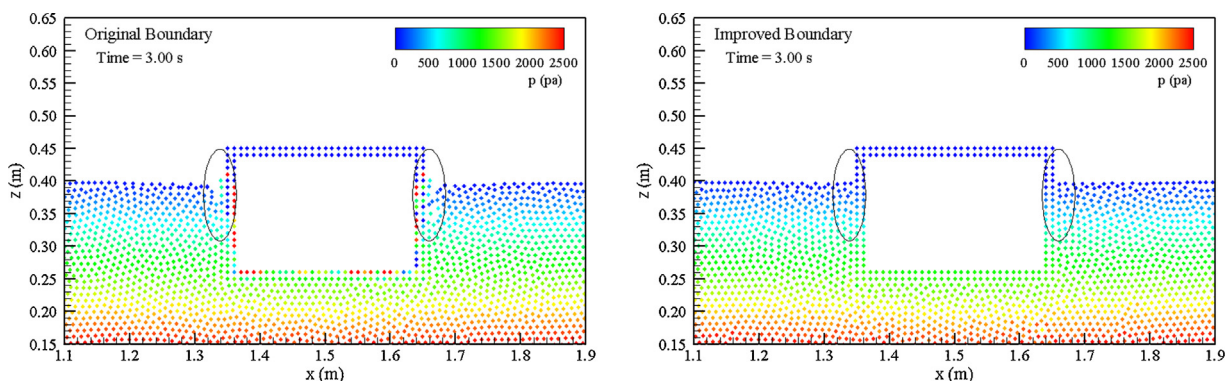


**Fig. 5.** Particle snapshots of the vertically oscillating box at  $t = 3.00$  s. Left: original DBPs. Right: improved DBPs.

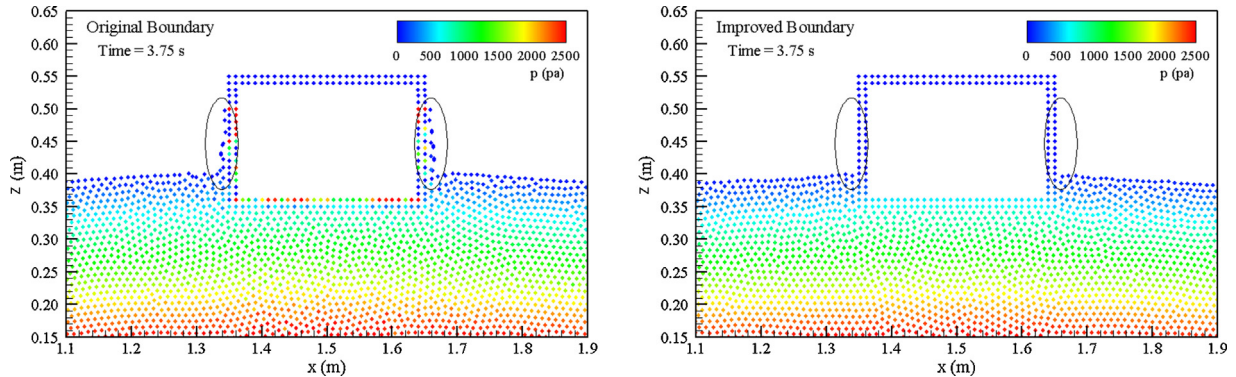


**Fig. 6.** Particle snapshots of the vertically oscillating box at  $t = 3.75$  s. Left: original DBPs. Right: improved DBPs.

#### 4. Validation of the numerical model

##### 4.1. Vertical oscillation of a rectangular box

As mentioned in the section of boundary treatment, when applying the original DBPs on the solid boundary, spurious high-frequency pressure oscillations and large unphysical boundary layers can appear in the flow near the solid wall. The unphysical boundary layers are particularly obvious when fluid particles sliding along the boundaries. To minimize this spurious effect, the calculated densities of DBPs are buffered by the mean densities of the fluid particles in the vicinity of the boundary shown as Eqs. (11) and (12).

In this section, the forced vertical oscillation of a rectangular box with the amplitude of 0.05 m and the period of 1.5 s in still water is investigated to validate the proposed algorithm of the solid boundary treatment. As shown in Fig. 3, the NWT is 3 m long and 0.8 m high. The water depth is 0.4 m. A rectangular box of width  $B_f = 0.30$  m and height  $H_f = 0.20$  m is placed in the flume. The box is homogeneous, and its center of mass coincides with its geometric center. A total of 12,580 particles including 926 fixed boundary particles and 192 moving boundary particles are used in the simulation, with an initial spacing of 0.01 m. The smoothing length  $h$  used in this paper is 1.3 times of the initial particle spacing.

Since vertical motion of the box generates scattering waves propagating to both sides of the wave flume, two 1-m-long damping layers are placed at both ends of the flume to absorb the propagating waves. In the two damping zones, artificial damping

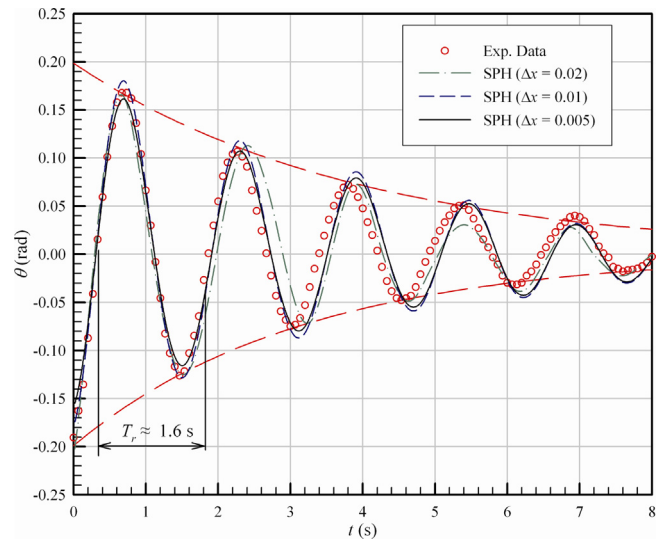


**Fig. 7.** Time history of the roll angle during the damped rolling oscillation ( $\Delta x$  is the initial particle spacing).

term  $\mu(x)\mathbf{u}_i$  is added to the momentum equation (Eq. (5)).  $\mu(x)$  is adopted as the following linear expression

$$\mu(x) = \alpha \frac{|x - x_0|}{l_s} \quad x_0 < x < x_0 + l_s \quad (25)$$

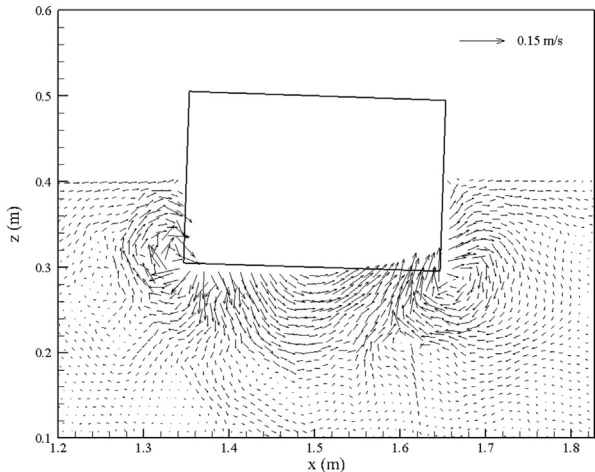
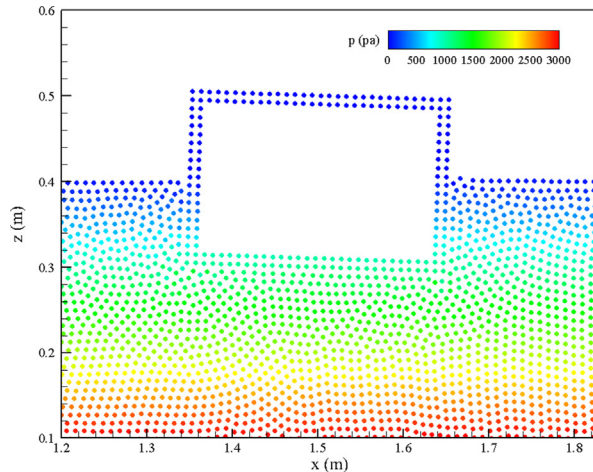


**Fig. 8.** Particle distribution and velocity vector speed near the rolling box.

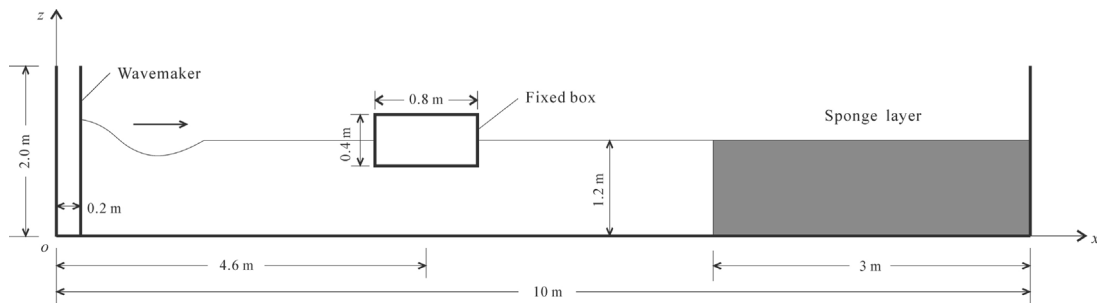


**Fig. 9.** Sketch of the test case with regular waves on a fixed rectangular box.

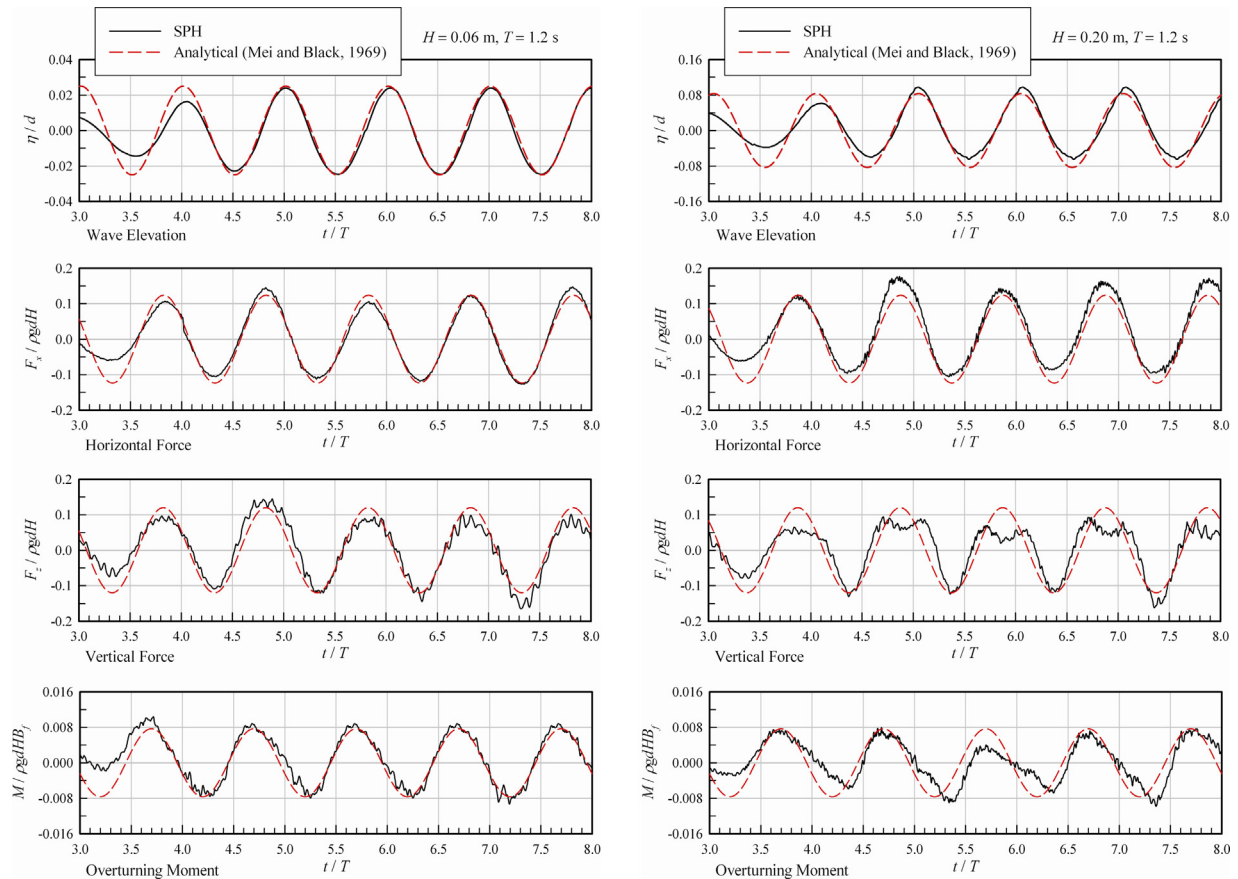
where  $l_s$  is the length of the sponge layer,  $x_0$  is the horizontal position where scattering waves initially enter into the damping layer,  $\alpha$  equals to 4.

In this case, the oscillation is restricted in the vertical direction, and therefore the horizontal force and the overturning moment about the body centroid exerted by fluid should be zero. However, the calculated results are nonvanishing due to the spurious numerical high-frequency oscillation of pressure. Fig. 4 shows the calculated horizontal force  $F_x$  and the overturning moment  $M$  on the box using the original DBPs and the improved DBPs. It can be seen that the calculated results using the original DBPs present random fluctuations around zero with the maximum amplitude of horizontal force up to 100 N and the maximum overturning moment up to 6 N m, while employing the improved DBPs, the maximum horizontal force is about 10 N and the maximum overturning moment is less than 0.4 N m, which demonstrates that the disturbing force

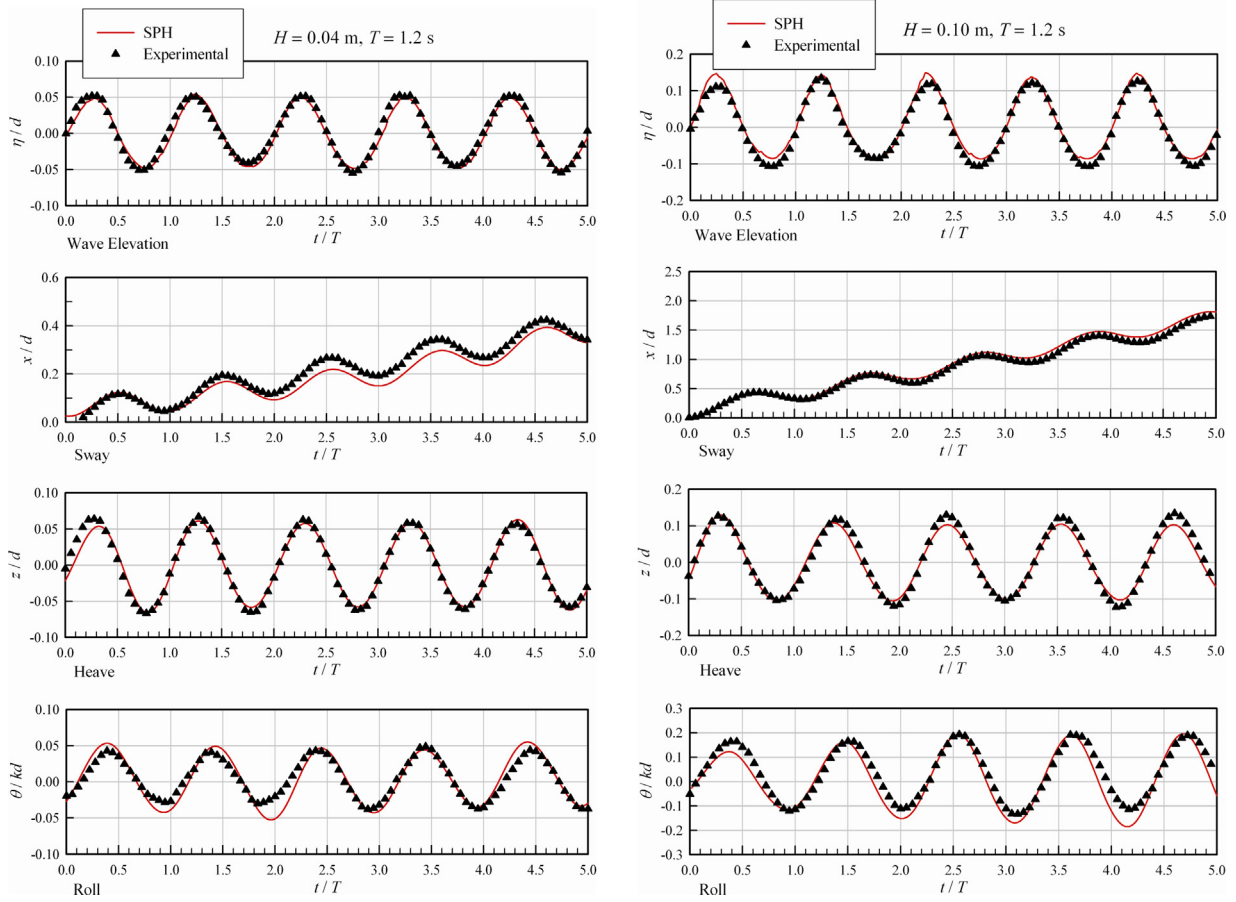
in both directions can be reduced by up to one order of magnitude using the improved DBPs boundary.

Fig. 5 shows the particle snapshots of the vertically oscillating box with pressure fields at  $t = 3.00$  s. At this moment, the box sinks to the lowest position. The discontinuity of particle pressures near the body boundary and an obvious unphysical layer are observed in the left plot using the original DBPs, especially the pressures of the boundary particles on the inner row are significantly larger than that of the nearby particles. While in the right plot using the improved DBPs, the particle pressures near or on the body boundary are observed to be continuous and no fluid particles are separated from the box boundary.

Fig. 6 shows the particle snapshots of this test case at  $t = 3.75$  s. At this moment, the box is located at the highest position. When using the original DBPs as shown in the left plot of Fig. 6, the particle pressures near or on the body boundary are seen to be



**Fig. 10.** Comparison of wave elevations and filtered wave forces on a fixed rectangular box between SPH and analytical solution. Left:  $H = 0.06 \text{ m}$ ,  $T = 1.2 \text{ s}$ . Right:  $H = 0.20 \text{ m}$ ,  $T = 1.2 \text{ s}$ .



**Fig. 11.** Time histories of the motion trajectories of the free-floating box under regular waves. Left:  $H = 0.04 \text{ m}$ ,  $T = 1.2 \text{ s}$ . Right:  $H = 0.10 \text{ m}$ ,  $T = 1.2 \text{ s}$ .

noncontinuous and a number of fluid particles are adhered to the body boundary even when the body is out of the water. It can be seen from Figs. 5 and 6, using the original DBPs always results in a presence of a row of fluid particles subject to the attraction by the boundary particles due to the inappropriate pressure gradient between the boundary particles and the fluid particles. The right plot of Fig. 6 shows that when using the improved algorithm of DBPs, the pressure field is continuous and no fluid particles adhered to the body boundary.

#### 4.2. Damped rolling oscillation of a floating box

In this section, the damped oscillation of a floating box in the rolling degree of freedom is studied. It is known that the viscous damping is the dominant damping mode in the roll motion of a floating body. The aim of studying this case is to examine the artificial viscosity adopted and check the convergence of the numerical model. The Monaghan [34] type artificial viscosity  $\Pi_{ij}$  in SPH models provide the necessary dissipation to convert kinetic energy of fluid into heat, which successfully reduce the unphysical pressure oscillation in WSPH. Also, it introduces a shear viscosity into the flows, thus endowing the momentum equation (Eq. (5)) with the character of viscous flow. In this paper, the quadratic term in  $\Pi_{ij}$  is neglected, so the value of  $\alpha_\Pi$  dominates the viscosity in the SPH. Here the reference value of  $\alpha_\Pi = 0.01$  is used.

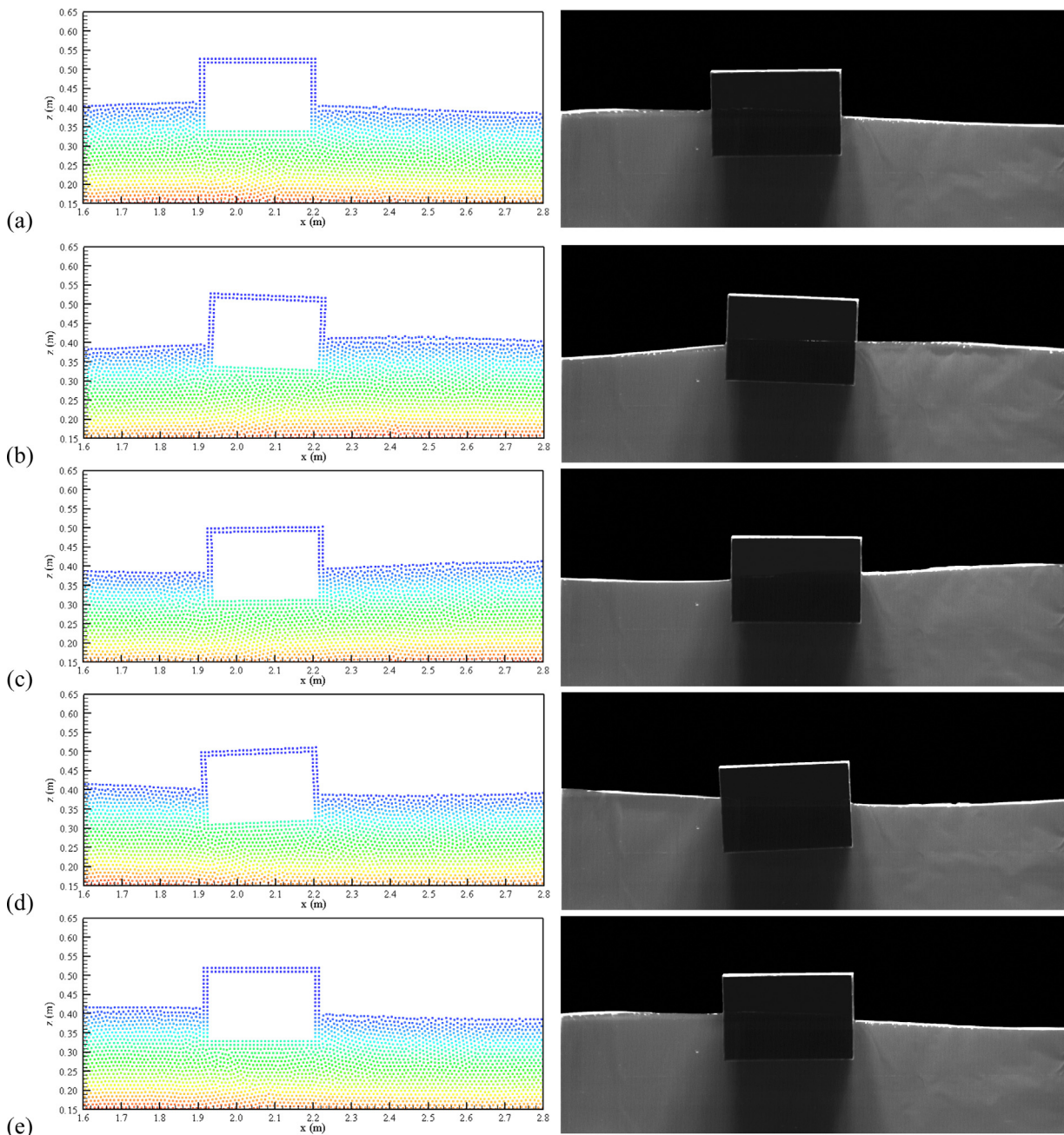
The damped oscillation is performed in the same NWT as built in Section 4.1. The dimension of the box and other relevant parameters are also the same as those defined in Section 4.1. The floating box is homogeneous and its centroid is fixed at point (1.5, 0.4), and the initial angle of inclination  $\theta_0$  is  $15^\circ$ .

Fig. 7 shows the comparison of the time history of roll angles between the computed results with different spatial resolutions and the experimental data. The red dash line represents the envelope curves of measured rolling amplitudes. The experimental rolling period  $T_r$  is about 1.6 s. As shown in Fig. 7, for  $\Delta x = 0.02$ , a faster attenuation of rolling amplitude is observed and the rolling period is not as rhythmical as that of the experimental data. When  $\Delta x = 0.01$  and 0.005, the rolling amplitudes and natural rolling periods are well reproduced. Considering the computational efficiency, fluid particles spacing of 0.01 m are used for all simulations presented in this paper. Following the computation method by Antuono [16], the convergence rate for the current numerical model is 1.68. The results also indicates that  $\alpha_\Pi = 0.01$  is a satisfactory choice in terms of the size and the type of the floating box investigated in this paper.

In addition, snapshots and velocity field of the floating box for the case of  $\Delta x = 0.01$  are given in Fig. 8. As it can be seen flow separation and vortex generation are well simulated including the areas near the immersed corners of the floating box.

#### 4.3. Wave forces on a fixed rectangular box

In this section, an investigation of wave forces on a fixed rectangular box is conducted to verify the accuracy of the computed wave forces. The NWT (Shown in Fig. 9) is 10 m long and 1.8 m high with water depth of 1.2 m. A rectangular box of breadth  $B_f = 0.80 \text{ m}$  and height  $H_f = 0.40 \text{ m}$  is fixed and semi-immersed, and its centroid is located at point (4.6 m, 1.2 m). Approximately 96,500 particles including 2326 fixed boundary particles and 360 moving boundary



**Fig. 12.** Floating box locations and ambient wave surfaces of SPH calculations (left figure), compared with experimental photos (right figure) for  $H=0.04$  m,  $T=1.2$  s. (a)  $t=t_0$ , (b)  $t=t_0+T/4$ , (c)  $t=t_0+T/2$ , (d)  $t=t_0+3T/4$  and (e)  $t=t_0+T$ .

particles are used in the simulations, with an initial particle spacing of 0.01 m.

An active absorbing piston-type wave maker [36] is set at  $x=0.2$  m initially to generate propagating waves. An artificial damping layer as used in Section 4.1 is arranged at the downstream boundary of the NWT to absorb the outgoing waves. The length of the damping layer is approximately equal to one wavelength.

The analytical solution using the frequency domain method obtained by Mei and Black [37] under two different wave steepness are used as comparison, which are converted to duration curve by multiplying it by a time function  $\cos(\omega t)$ . Fig. 10 shows the comparison between our computed results and the analytical solution. The computed wave elevations  $\eta$  are measured at the position  $x=4.6$  m while the box is not placed in the tank.

For the case of  $H=0.06$  m,  $T=1.2$  s, the relative water depth  $d/L$  is 0.54 and the relative wave height  $H/L=0.027$ , which indicates the incoming waves can be nearly regarded as a linear wave. As can be seen from Fig. 10, the computed wave elevation is almost identical with the analytical solution. The horizontal wave force  $F_x$ , the vertical force  $F_y$  and the overturning moment about the centroid  $M$  agree fairly well with the analytical solution except that the computed wave forces have a little nonphysical fluctuations, which demonstrates that the amplitudes of the wave forces are well simulated by the improved boundary treatment.

For the case of  $H=0.20$  m,  $T=1.2$  s, the relative water depth  $d/L$  is 0.54 and the relative wave height  $H/L=0.089$ , so the linear theory is not suitable for this case. Poor agreements are observed between the calculated results (wave elevation and wave forces including horizontal forces  $F_x$ , vertical forces  $F_z$  and overturning moment  $M$ )

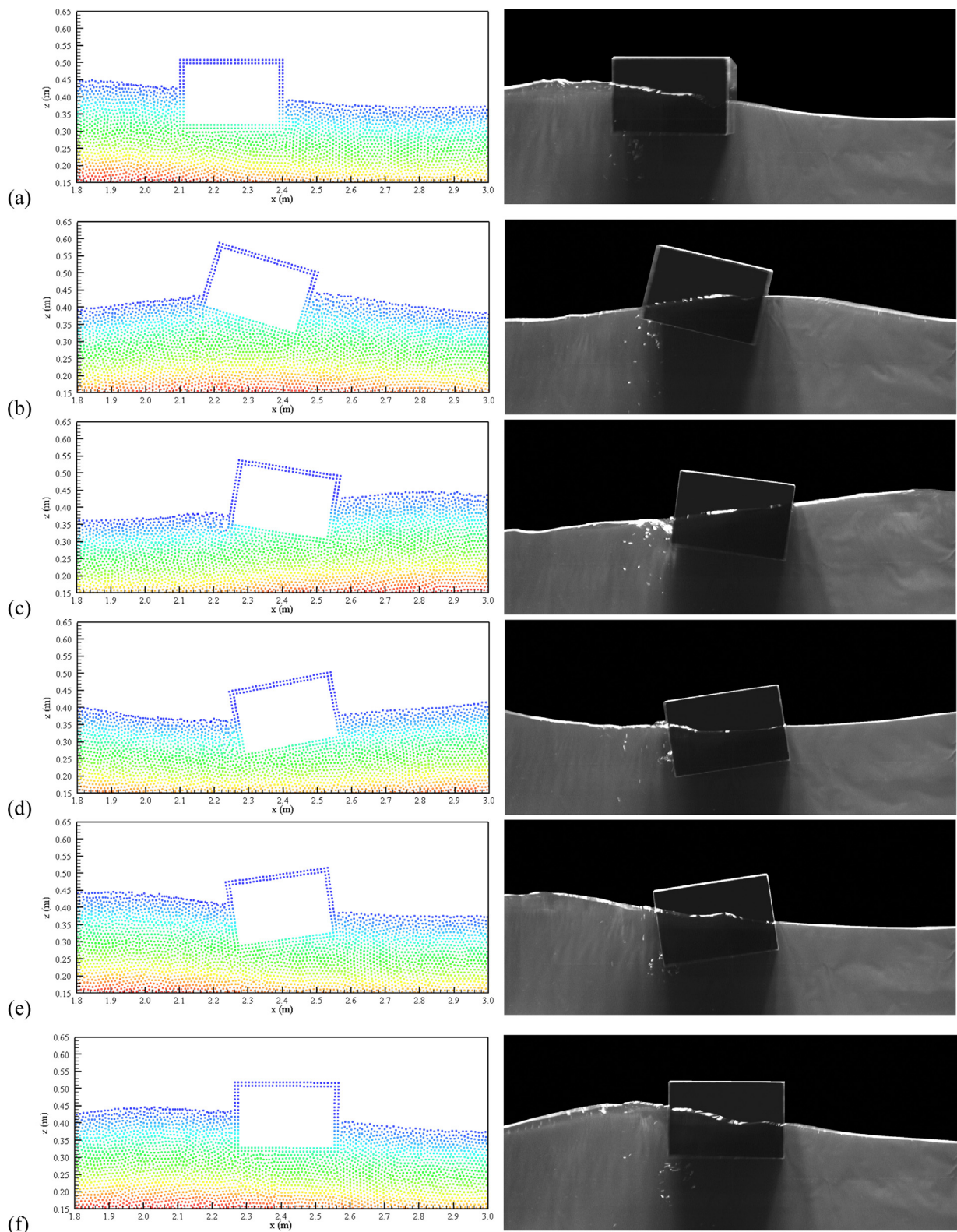


**Fig. 13.** Floating box locations and ambient wave surfaces of SPH calculations (left figure), compared with experimental photos (right figure) for  $H = 0.10$  m,  $T = 1.2$  s. (a)  $t = t_0$ , (b)  $t = t_0 + T/4$ , (c)  $t = t_0 + T/2$ , (d)  $t = t_0 + 3T/4$ , (e)  $t = t_0 + T$  and (f)  $t = t_0 + 1.09T$ .

and the analytical solutions based on linear theory. As can be seen from the right plot of Fig. 10, though the computed wave height and period by the present improved WCSPH model at the measuring point are consistent with the linear waves, the wave profiles are not identical with the sinusoidal curve. The computed wave profile

has sharp wave crest and flat wave trough, which conforms to the surface character of a nonlinear wave. The same nonlinearity can be observed in the plot of the horizontal force. A double-hump curve is observed in the time history of the vertical wave force, which also implies significant nonlinearity of wave forces.

## 5. Motions of a free floating box in waves

In this section, the NWT illustrated in Fig. 9 with a different water depth of 0.4 m is used to study the motions of a free floating box under regular waves. The floating box is 0.30 m in breadth and 0.20 m in height. Its centroid initially locates at point (2.0 m, 0.4 m) and it can move in three degrees of freedom as sway, heave and roll without any constraint. Using the present improved WCPH model, we calculate the motion trajectories of a free-floating box under regular waves with different wave heights ( $H = 0.04 \text{ m}$ ,  $T = 1.2 \text{ s}$  and  $H = 0.10 \text{ m}$ ,  $T = 1.2 \text{ s}$ ). The motions of the floating box are presented in Fig. 11. A reference system  $o-xz$  is defined, with  $x$  positive rightwards and  $z$  positive upwards. The  $\theta$  in this section donates the roll angle which is positive in the clockwise direction.

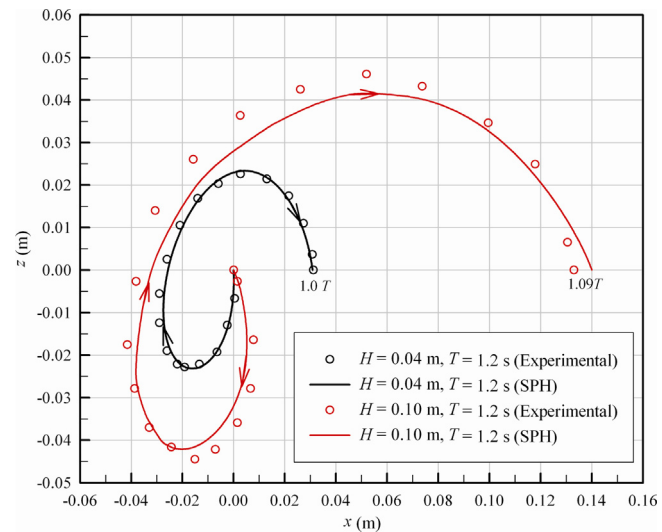
From Fig. 11, it can be seen that the agreements of motion trajectories between SPH simulations and experimental data are satisfactory. The heave components present simple harmonic oscillations, and it is the same for the roll components. As for the sway motion, simple harmonic oscillations combining with drifting motions in the  $x$  direction can be seen. The drifting motions in the  $x$  direction are due to the mean drift forces. According to the research by Mauro [38], the mean drift force on the floating body is proportional to the square of  $H_\sigma$ , which is the sum of the reflected wave height and the scattered wave height due to the moving body. It is not difficult to know that  $H_\sigma$  has positive correlation with the incident wave height; therefore the sway motion of the case  $H = 0.12 \text{ m}$  show obviously larger drifting speed than that of the case  $H = 0.04 \text{ m}$ .

Fig. 12 shows the calculated and experimental results of the positions of the floating box at various representative instants ( $t_0$ ,  $t_0 + T/4$ ,  $t_0 + T/2$ ,  $t_0 + 3T/4$  and  $t_0 + T$ ) in a wave period, where  $t_0$  is the initial time when the box is in horizontal position. The wave condition in the figure is  $H = 0.04 \text{ m}$ ,  $T = 1.2 \text{ s}$ .

From Fig. 12, it can be seen that the computed positions of the box as well as wave surfaces are in good agreements with the experimental results. The box firstly rotates clockwise and drifts rightwards with the coming wave from left. Then, following the rising of wave surface on the right-hand side and the falling on the left, it rotates anti-clockwise and returns to horizontality at  $t_0 + T/2$ . Under the action of inertia force, it continues to rotate anti-clockwise and drift leftwards. From  $t_0 + 3T/4$ , it begins to rotate clockwise, and finally, it nearly returns to nearly horizontality at  $t_0 + T$  with the next coming wave from left. Comparing the horizontal positions of the box at  $t_0$  and  $t_0 + T$ , it can be seen that the floating box drifts with a small displacement to the right.

Fig. 13 shows the calculated and experimental results of positions of the floating box when the wave height is comparatively large ( $H = 0.10 \text{ m}$ ,  $T = 1.2 \text{ s}$ ). The agreement between the computed results and experimental results is still acceptable, although the computed wave surface on the left-hand side of the box is a little lower than the measured data at  $t_0$  and  $t_0 + T$ . Two notable differences from the case of  $H = 0.04 \text{ m}$  can be observed. One is that the floating box does not return to horizontality at  $t_0 + T/2$  and  $t_0 + T$ , which indicates that the motion period  $T_m$  does not coincide with the incoming wave period. The floating box returns to horizontality at  $t_0 + 1.09T$ , so the motion period of the box is  $1.09T$ . The other one is that the drift displacement is obviously larger than that of the case of  $H = 0.04 \text{ m}$ . The drift displacement is about 0.14 m.

Fig. 14 shows the centroid trajectories of the floating box in a motion period under the two wave conditions. The  $x$  coordinate represents the horizontal displacement of the centroid of the floating box while the  $z$  coordinate represents the vertical displacement. It can be seen that the floating box returns to the initial horizontal position with a drift displacement in the  $x$  direction after a motion period. The drift displacement of  $H = 0.04 \text{ m}$  is 0.03 m and



**Fig. 14.** Centroid trajectories of the floating box in motion period (SPH, solid curve; experimental data, ○).

that of  $H = 0.10 \text{ m}$  is  $0.14 \text{ m}$ . The motion period  $T_m$  is the same as the incoming wave period  $T$  when  $H = 0.04 \text{ m}$ , while  $T_m$  equals to  $1.09T$  when  $H = 0.10 \text{ m}$ . Thus, a phenomenon that a larger wave height leads to a larger motion period is observed.

The reason for this phenomenon is the relative motion between the wave and floating box. For example, at the initial time  $t_0$ , if the box is at the wave crest and the rolling angle is max. Then the box rolls periodically with the rightwards transmission of wave. If there is no drift motion in the horizontal direction, the box should return to the initial state at  $t_0 + T$ , and the motion period  $T_m$  will be equal to wave period  $T$ . But if there is drift motion in the horizontal direction, at  $t_0 + T$ , the box is in front of the wave crest due to the drift motion and it has not rotated to the initial rolling angle yet. Therefore it requires extra more time ( $T_m - T$ ) to complete a motion period. Generally the motion period  $T_m$  increases with the increasing drift speed of the floating body. Since the drift speed increases with the increasing nonlinearity of wave, the motion period has a positive relationship with the nonlinearity of incident wave.

## 6. Conclusions

A new algorithm based on DBPs in the frame of WCPH is proposed to evaluate the forces exerted on the boundary particles exerted by the neighboring fluid particles. The calculated pressures of DBPs are averaged by the mean pressures of fluid particles in their kernel supports to reduce the spurious effects.

The proposed boundary algorithm proves to be robust in solving problem of the vertical oscillation of a rectangular box. In comparison with the original DBPs, the results of the improved DBPs are much better without the obvious phenomena such as high-frequency force oscillations, the large boundary layers and the unphysical attraction by the DBPs when the body is out of water. The amplitudes of the wave forces on the fixed body are also well simulated by the improved boundary treatment.

The full coupling between waves and a free floating rectangular box is well simulated using the proposed model. The motion components, the position and inclinations changes and the centroid trajectories of the floating box show good agreements with the experiment data. More extensive numerical tests would be required to confirm its applicability for floating bodies with complex geometries.

## Acknowledgements

The improved WCSPH code using in this paper was developed from the open source SPHysics code developed by Prof. Robert A. Dalrymple at Johns Hopkins University, Prof. Moncho Gómez-Gesteira at Univ. de Vigo, and others.

This work was funded by the National Natural Science Foundation of China under Grant No. 51179030 and Innovative Research Group of the National Natural Science Foundation of China under Grant No. 51221961.

## References

- [1] Teng B, Taylor RE. A BEM method for the second-order wave action on a floating body in monochromatic waves. In: International conference on hydrodynamics. 1994. p. 274–81.
- [2] Longuet-Higgins MS, Cokelet ED. The deformation of steep surface waves on water: I. A numerical method of computation. Proc R Soc A Math Phys Eng Sci 1976;350:1–26.
- [3] Faltinsen OM. Numerical solution of transient nonlinear free-surface motion outside or inside moving bodies. In: Proceedings of the 2nd international conference on numerical ship hydrodynamics. 1977. p. 257–66.
- [4] Vinje T, Breivig P. Nonlinear ship motions. In: Proceedings of the 3rd international conference on numerical ship hydrodynamics. 1981. p. 257–66.
- [5] Kashiwagi M. Non-linear simulations of wave-induced motions of a floating body by means of the mixed Eulerian-Lagrangian method. Proc Inst Mech Eng C 2000;214:841–55.
- [6] Koo W, Kim M-H. Freely floating-body simulation by a 2D fully nonlinear numerical wave tank. Ocean Eng 2004;31:2011–46.
- [7] Hadžić I, Hennig J, Perić M, Xing-Kaeding Y. Computation of flow-induced motion of floating bodies. Appl Math Model 2005;29:1196–210.
- [8] Jung JH, Yoon HS, Chun HH, Lee I, Park H. Numerical simulation of wave interacting with a free rolling body. Int J Naval Archit Ocean Eng 2013;5: 333–47.
- [9] Hu C, Kashiwagi M. Two-dimensional numerical simulation and experiment on strongly nonlinear wave–body interactions. J Mar Sci Technol 2009;14:200–13.
- [10] Monaghan JJ. Smoothed particle hydrodynamics. Annu Rev Astron Astrophys 1992;30:543–74.
- [11] Monaghan JJ, Kos A, Issa N. Fluid motion generated by impact. J Waterw Port Coast Ocean Eng 2003;129:250–9.
- [12] Doring M, Oger G, Alessandrini B, Ferrant P. SPH simulations of floating bodies in waves. In: Proceedings of the 23rd international conference on offshore mechanics and arctic engineering. 2004. p. 741–7.
- [13] Shao S, Gotoh H. Simulating coupled motion of progressive wave and floating curtain wall by SPH-LES model. Coast Eng J 2004;46:171–202.
- [14] Omidvar P, Stansby PK, Rogers BD. SPH for 3D floating bodies using variable mass particle distribution. Int J Numer Methods Fluids 2013;72:427–52.
- [15] Hashemi MR, Fatehi R, Manzari MT. A modified SPH method for simulating motion of rigid bodies in Newtonian fluid flows. Int J Non-Linear Mech 2012;47:626–38.
- [16] Antuono M, Colagrossi A, Marrone S, Lugni C. Propagation of gravity waves through an SPH scheme with numerical diffusive terms. Comput Phys Commun 2011;182:866–77.
- [17] Bouscasse B, Colagrossi A, Marrone S, Antuono M. Nonlinear water wave interaction with floating bodies in SPH. J Fluids Struct 2013;42:112–29.
- [18] Dalrymple RA, Knio O. SPH modelling of water waves. In: Proceedings of coastal dynamics 2001. 2001. p. 779–87.
- [19] Crespo AJC, Gómez-Gesteira M, Dalrymple RA. Boundary conditions generated by dynamic particles in SPH methods. Comput Mater Continua 2007;5:173–84.
- [20] Colagrossi A, Landrini M. Numerical simulation of interfacial flows by smoothed particle hydrodynamics. J Comput Phys 2003;191:448–75.
- [21] Oger G, Doring M, Alessandrini B, Ferrant P. Two-dimensional SPH simulations of wedge water entries. J Comput Phys 2006;213:803–22.
- [22] Monaghan JJ. Simulating free surface flows with SPH. J Comput Phys 1994;110:399–406.
- [23] Monaghan JJ, Kos A. Solitary waves on a Cretan beach. J Waterw Port Coast Ocean Eng 1999;125:145–54.
- [24] Rogers BD, Dalrymple RA. SPH modeling of tsunamis. In: Advances in coastal and ocean engineering. World Scientific; 2008. p. 75–100.
- [25] Liu X, Lin P, Shao S. An ISPH simulation of coupled structure interaction with free surface flows. J Fluids Struct 2014;48:46–61.
- [26] Shao S. Incompressible SPH simulation of water entry of a free-falling object. Int J Numer Methods Fluids 2009;59:91–115.
- [27] Monaghan JJ, Kajtar JB. SPH particle boundary forces for arbitrary boundaries. Comput Phys Commun 2009;180:1811–20.
- [28] Marrone S, Antuono M, Colagrossi A, Colicchio G, Le Touzé D, Graziani G. δ-SPH model for simulating violent impact flows. Comput Methods Appl Mech Eng 2011;200:1526–42.
- [29] Kajtar J, Monaghan JJ. SPH simulations of swimming linked bodies. J Comput Phys 2008;227:8568–87.
- [30] Gómez-Gesteira M, Cerqueiro D, Crespo C, Dalrymple R. Green water overtopping analyzed with a SPH model. Ocean Eng 2005;32:223–38.
- [31] Wendland H. Piecewise polynomial, positive definite and compactly supported radial functions of minimal degree. Adv Comput Math 1995;4:389–96.
- [32] Monaghan J. Particle methods for hydrodynamics. Comput Phys Rep 1985;3:71–124.
- [33] Dalrymple RA, Rogers BD. Numerical modeling of water waves with the SPH method. Coast Eng 2006;53:141–7.
- [34] Monaghan J. On the problem of penetration in particle methods. J Comput Phys 1989;82:1–15.
- [35] Monaghan JJ. Smoothed particle hydrodynamics. Rep Prog Phys 2005;68:1703–59.
- [36] Hirakuchi H, Kajima R, Kawaguchi T. Application of a piston-type absorbing wave-maker to irregular wave experiments. Coast Eng Jpn 1990;33:11–24.
- [37] Mei CC, Black JL. Scattering of surface waves by rectangular obstacles in waters of finite depth. J Fluid Mech 1969;38:499–511.
- [38] Mauro H. The drift of a body floating on waves. J Ship Res 1960;4:1–10.